

Unique hot-carrier distributions from scattering-mediated absorption

Jason Codrington[†], Noor Eldabagh[†], Kimberly Fernando[†], and Jonathan J. Foley IV*

Department of Chemistry, William Paterson University, 300 Pompton Road, Wayne, NJ,

07470, USA

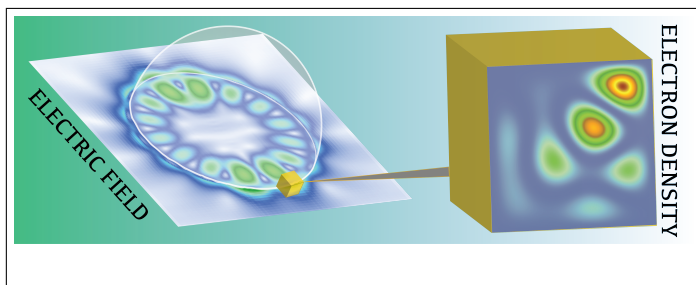
E-mail: foleyj10@wpunj.edu

*To whom correspondence should be addressed

Abstract

Light-initiated generation of energetic carriers has attracted considerable attention as a paradigm for photocatalysis and solar energy conversion, and the use of noble metal nanoparticles that support localized surface plasmon resonances has been widely explored as a medium for realizing this paradigm. It was recently shown that composite nanostructures that enable the interplay between dielectric scattering resonances and broad-band absorption in small metal nanostructures, a phenomenon termed scattering-mediated absorption, can be used to mediate energetic carrier transfer and selective photochemistry with low-intensity light while completely circumventing plasmon resonance. In this work, we develop a multi-scale modeling approach for elucidating the hot-carrier dynamics initiated by scattering mediated absorption. Our calculations reveal that unique hot carrier distributions and dynamics arise from scattering mediated absorption as compared plasmon excitation, and also suggest that in a variety of circumstances, scattering mediated absorption may lead to more efficient hot carrier generation than plasmon resonance under the same external illumination conditions. These results are an important first step in understanding the phenomena of scattering mediate hot carrier generation, which has potential for expanding the palette of materials that can be utilized for hot-carrier mediated photochemistry, and for enabling unique pathways for photocatalytic transformations.

Graphical TOC Entry



Introduction

Various strategies that exploit the optical properties of metal nanoparticles, namely their ability to support localized surface plasmons resonances [LSPR], which are collective oscillations of their conduction electrons driven by light, have been explored recently with the aim of using low-intensity light to efficiently drive chemical reactions.^{1–4} The interest in this area has been motivated partly by the fact that metal nanoparticles (most prominently silver and gold) are exceptionally good absorbers of visible light, so they are ideal candidates for harvesting solar photons.⁵ Importantly, the resonant properties of plasmonic particles are highly tunable by parameters under synthetic control such as geometry, composition, surface chemistry, and the surrounding environment.^{6–8} An emerging paradigm that exploits LSPR for photocatalysis is known as Plasmon-mediated Hot-Electron Transfer (PHET), and a growing number of reports are demonstrating the ability of PHET to catalyze energetically demanding chemical reactions.^{9–16} In PHET, the collective plasmon excitation decays rapidly (on a 10 femtosecond timescale) to a non-equilibrium distribution of energetic electron-hole pairs, or a so-called hot-electron distribution^{2,17–21} Hot-electrons can deposit energy into reactive degrees of freedom of molecules adsorbed to the nanoparticle surface, thereby initiating chemical transformations. Despite the considerable progress made in demonstrating the potential of the paradigm of PHET, its widespread application faces several challenges. The intrinsic optical properties of noble metals that give rise to the extraordinarily large absorption cross sections associated with LSPR are also fundamentally related to the broad energy spectra and short lifetimes associated with LSPR and the subsequent hot-electron distributions.²² Furthermore, the timescale of hot-electron relaxation competes with transfer to adsorbate states (both occur on 100 fs timescales), which fundamentally limits the efficiency of energy transfer.¹⁹ Finally, the most promising plasmonic materials typically have poor catalytic activity, and similarly, good catalytic metals typically are poor light harvesters.¹⁵

Considering this, an incredible opportunity exists to identify new classes of structures for mediating light-matter interactions and energy transfer events that offer the same ad-

vantages as metal nanoparticles, namely exceptional light-harvesting potential, while also offering greater selectivity and efficiency in energy transfer, as well as tunable surface chemistry for enhanced catalytic activity. Ideally, such structures could be made mostly, if not entirely, from cost-effective materials. Recent progress towards this aim has been made by designing hybrid nanostructures that effectively delegate the light-harvesting and catalytic functions to separate components of the structure. Recently, Halas and co-workers demonstrated an antenna-reactor concept that leverages the near-field enhancement from aluminum plasmons to generate energetic carriers on palladium islands and showed the efficacy of this strategy for the photocatalytic transformation of acetylene to ethylene.¹⁵ Two of the current authors, along with Sun and co-workers, demonstrated a phenomena known as scattering-mediated absorption where dielectric scattering resonances in SiO₂ ionospheres were utilized to induce resonant absorption in non-plasmonic platinum nanoparticles in SiO₂/Pt nanohybrids.¹³ The scattering-mediated absorption (SMA) phenomena was also observed to induce highly selective photocatalytic oxidation of benzyl alcohol to benzaldehyde.¹³ Zhang *et al.* independently described a SMA phenomenon in Au-TiO₂ nanohybrids that leveraged so-called whispering gallery modes to enhance plasmonic and non-plasmonic absorption in gold nanoparticles, and demonstrated these structures efficacy for photocatalytic water splitting.¹⁴ Interestingly, hot-carrier transfer was implicated in the photocatalytic mechanisms that resulted from these SMA phenomena.^{13,14} The prospect of using SMA in hybrid dielectric/metal nanostructures to initiate hot-carrier generation and transfer is particularly compelling as it could completely circumvent plasmon excitation. Not only does this open up possibilities to utilize a broader palette of materials, it also presents the possibility of realizing unique photocatalytic pathways owing to differences in the distributions and dynamics of energetic carriers produced by SMA compared to those produced by plasmon excitation.

The push to identify novel structures for mediating hot-carrier generation and transfer has been paralleled by efforts to develop theoretical methodologies to elucidate these processes. The underlying electronic structure has been treated both within free-electron models

confined by potential wells^{17,23–26} (here called “particle-in-a-well” [PIW] models), as well as by *ab initio* approaches.^{18,20,21,27} Using PIW models, Govorov and co-workers developed a theory of hot-electron generation within the framework of time-dependent perturbation theory that has elucidated a variety of shape- and size-dependent factors for optimizing the hot-carrier generation.^{17,23} A similar approach was also pursued by Kumarasinghe *et al.* suggesting that nanorods are exceptionally good structures for hot-carrier generation.²⁵ García de Abajo and co-workers recently described a quantum master equation approach with an underlying PIW model that elucidated a number of key factors that influence hot-carrier excitation and decay dynamics.²⁶ The utilization of *ab initio* approaches by Sundararaman *et al* has also provided valuable insights into the role that a metals band-structure plays in determining the efficiency of hot-carrier generation, and particularly in the asymmetry between hot-electron and hot-hole generation.¹⁸ Nordlander and co-workers have directly compared free-electron and *ab initio* approaches and found negligible impact on hot-carrier generation and dynamics in Ag nanospheres resulting from electron correlation,²⁴ though Bernardi *et al* have demonstrated that many-body effects are important in the hot-carrier dynamics resulting from surface plasmon polaritons in gold and silver.²⁷

We develop a novel approach for studying hot-carrier dynamics that may arise from arbitrary electromagnetic fields, including the unique near-fields that arise from SMA on hybrid dielectric-metal nanoparticles and LSPR on noble metal nanoparticles. We consider the electronic degrees of freedom on the metal nanoparticle subject to the time-dependent Hamiltonian

$$\hat{H}(t) = \hat{H}_{el} - \mathbf{E}(t) \cdot \hat{\mu}, \quad (1)$$

where the specific form of $\mathbf{E}(t)$ derives from a rigorous time-domain electrodynamics calculation with a realistic model of the nanostructures in question and \hat{H}_{el} describes non-interacting electrons confined to metal nanocubes [NCs] an infinite potential well. We compute the time-domain field using a commercial simulator based on the finite-difference time-domain [FDTD] method.²⁸ Incorporating $\mathbf{E}(t)$ from these FDTD simulations into the time-dependent Hamil-

tonian enables us to investigate the unique ways in which the electronic degrees of freedom evolve under the influence of the distinct time-varying fields that result from LSPR and dielectric scattering resonances, allowing us a unique window into the hot-carrier dynamics resulting from LSPR as compared to SMA. More details about the FDTD calculations are provided in the supplemental information.

The many-electron wavefunction of the metal nanoparticles is expanded in terms of a configuration-interaction expansion that includes all singly-excited configurations,

$$|\Psi_{CIS}\rangle = c_0|\Phi_0\rangle + \sum_{i,a} c_i^a |\Phi_i^a\rangle, \quad (2)$$

where the configuration $|\Phi_i^a\rangle$ has an electron excited from orbital i to orbital a , and c_0 and c_i^a are complex expansion coefficients. Unless otherwise specified, indices i, j will indicate orbitals which are occupied in the ground state reference configuration and indices a, b will indicate orbitals which are unoccupied in the ground state reference.

The time-evolution of the wavefunction can be subsumed in the expansion coefficients, which allows the TDSE to be written

$$i\hbar \frac{d}{dt} \mathbf{c}(t) = \mathbf{H}(t) \mathbf{c}(t) \quad (3)$$

where $\mathbf{c}(t)$ is the vector of complex expansion coefficients and $\mathbf{H}(t)$ is the time-dependent Hamiltonian matrix. The Hamiltonian matrix is comprised of three unique blocks in the CIS model,

$$\mathbf{H}(t) = \begin{pmatrix} \langle \Phi_0 | \hat{H}(t) | \Phi_0 \rangle & \langle \Phi_0 | \hat{H}(t) | \Phi_i^a \rangle \\ \langle \Phi_j^b | \hat{H}(t) | \Phi_0 \rangle & \langle \Phi_j^b | \hat{H}(t) | \Phi_i^a \rangle \end{pmatrix}. \quad (4)$$

Explicit expressions for Hamiltonian matrix elements are given for the NC model in the supplemental information.

Given the simplicity of the underlying electronic Hamiltonian, the field-free Hamiltonian matrix is diagonal, and only the dipolar interaction of the nanoparticle with the external

field can induce transitions among the electronic configurations, hence the treatment in this work neglects excited-state decay contributions from electron-electron scattering. These contributions will be explored in future work. Also because of the diagonal nature of field-free Hamiltonian, each configuration $|\Phi_i^a\rangle$ is an eigenfunction of the field-free Hamiltonian. This simplifies the interpretation of the electronic structure relative to the CIS wavefunction in molecular quantum mechanics where electron repulsion is included in the Hamiltonian and the excited electronic eigenfunctions are linear combinations of singly-excited configurations. The multiplication of the Hamiltonian matrix on the coefficient vector generates the gradient of the coefficient vector in time, and a variety of algorithms are known that use this information to propagate the wavefunction in time. Here we use a symplectic integrator described in Ref. 29. Propagation of the CIS wavefunction is referred to as the TDCIS method throughout.

We analyze the hot-carrier distribution and dynamics that results from SMA and LSPR excitation by computing the instantaneous populations of orbitals both above and below the Fermi level of the metal nanostructure. In our model, the orbitals are energy eigenstates of a 1-electron Hamiltonian and have well-defined kinetic energy, and the orbital populations are given by the diagonal elements of the 1-electron reduced density matrix,

$${}^1D_q^q(t) = \langle \Psi(t) | \hat{a}_q^\dagger \hat{a}_q | \Psi(t) \rangle, \quad (5)$$

where the second-quantized operator \hat{a}_q^\dagger (\hat{a}_q) creates (kills) an electron in orbital q . The orbital indices can be uniquely mapped to the relevant orbital quantum numbers (n_x, n_y, n_z for the PIW model for nanocubes) so that the orbital energies can be readily computed.

The TDCIS approach is applied to investigate hot-carrier dynamics of $L = 2\text{nm}$ gold and platinum NCs that are (a) free-standing so that the dynamics are induced by optical resonances supported by the NC alone and (b) supported on various dielectric nanospheres so that the dynamics are also induced by time-evolving nearfields arising from dielectric

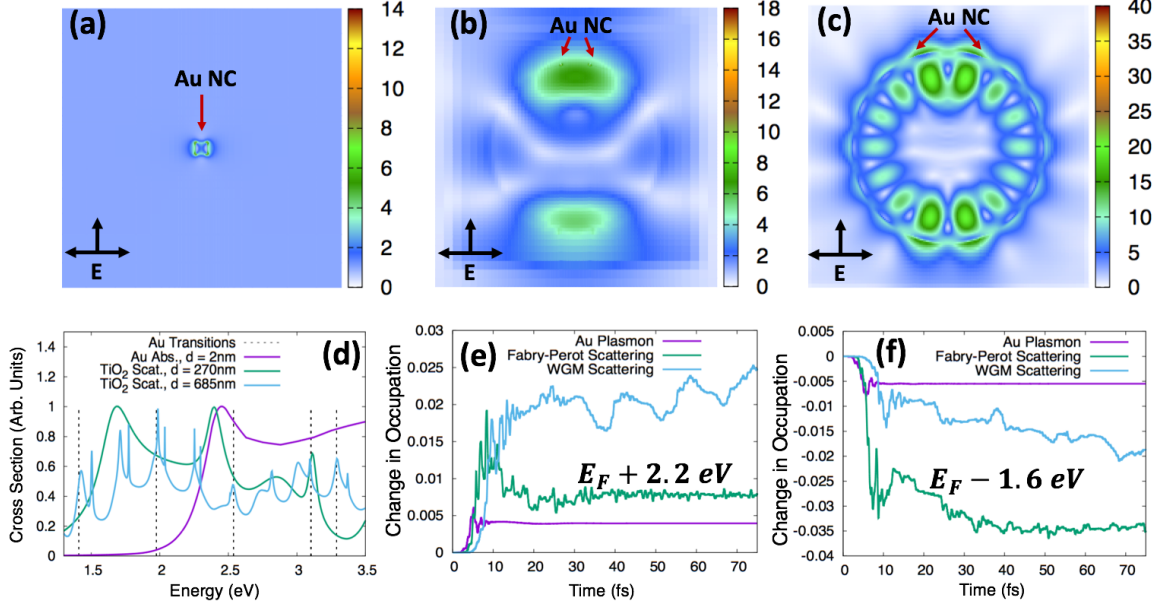


Figure 1: Three regimes for light-matter interactions leading to unique spatial and temporal shaping of the incident field, and the corresponding impact on electronic dynamics in a Au nanocube. Plots of the near-field enhancements ($|E|/|E_0|$) are shown of the Au NCs LSPR ($\lambda = 532\text{nm}$, **Panel (a)**), a Fabry-Perot resonance of a $d=285\text{nm}$ dielectric nanosphere decorated with Au NCs ($\lambda = 397\text{nm}$, **Panel (b)**), and a Whispering Gallery Mode resonance of a $d=685\text{ nm}$ dielectric nanosphere decorated with Au NCs ($\lambda = 493\text{nm}$, **Panel (c)**). The extinction spectra of these three structures are shown overlaid with the dipole-allowed transitions in the PIW model of the Au NC, showing particularly strong overlap between these transitions and the scattering resonances of the $d=685\text{ nm}$ dielectric nanosphere (**Panel (d)**). The change in orbital populations ($D_p^p(t) - D_P^p(t = 0)$) is computed to measure hot-electron and hot-hole generation. Both dielectric scattering resonances show more efficient generation of hot-electrons (**Panel (e)**) and hot-holes (**Panel (f)**) compared to LSPR in this case.

scattering resonance. The electronic structure of these model NCs are distinguishable by their Fermi energies and the number of electrons: the Au NC model has a Fermi energy of 5.52 eV (compared to the bulk value of 5.53 eV) and 472 electrons, the Pt NC model has a Fermi energy of 9.40 eV (compared to the bulk value of 9.75 eV) and 1104 electrons. In this work, 4900 singly-excited configurations are included in $|\Psi_{CIS}\rangle$ for both Au and Pt NCs. Despite the large number of excited states included in our many-electron wavefunctions, the high degeneracy of the underlying dipole-allowed transitions leads to a relatively small number of visible spectroscopic lines for the Au (see Figure 1 (d)) and Pt models (see Figure 2 (d)).

The spectral flexibility of dielectric scattering resonances allows tuning to overlap with one or more of these transition energies via the nanosphere size; in contrast, for very small metal nanoparticles, the position of the LSPR is intrinsically related to the relative permittivity of the metal.³⁰ This is illustrated by plotting the scattering spectrum of a moderate-sized ($d = 270\text{nm}$) and large ($d = 685\text{nm}$) dielectric nanospheres and the absorption spectrum of a small ($d = 2\text{nm}$) gold nanosphere overlaid with the dipole-allowed transitions in our PIW model of the Au NC (see Figure 1(d)). The $d = 270\text{nm}$ dielectric nanosphere has a relatively broad scattering resonance (herein referred to as a Fabry-Perot [FP] resonance) that overlaps with an Au transition at 3.1 eV, and a $d = 685\text{nm}$ dielectric nanosphere has narrow scattering resonances (whispering gallery modes [WGM]) that overlap with multiple transitions between 1.3 and 3.3 eV. The 2nmAu NC has a broad absorption peak associated with its LSPR that partially overlaps with a dipole-allowed transition in the PIW Au NC at 2.5 eV. As proxies of the hot-carrier dynamics in the Au NC, we plot the population dynamics of the highest and lowest energy orbitals in our active space, which lie 2.2 eV above and 1.6 eV below the Fermi energy, respectively (Figure 1 (e) and (f)). Snapshots of the populations of all active orbitals in the Au NC model at various times are also provided in the supplemental information (see Figure S1). We observe that the LSPR generates a relatively small population of hot-carriers with field-driven dynamics that evolve on a short

(10 fs) timescale. FP resonance in this case lead to significantly more efficient hot-hole generation with field driven dynamics that evolve on a moderate (50 fs) timescale (Figure 1(f)), while WGM resonances lead to significantly more efficient hot-electron generation with field drive dynamics that evolve on a much longer (200 fs) timescale (Figure 1(e) and Figure 3(b)). Another key distinction hot-carrier density generated by the Au LSPR and by SMA is that the hot-carrier density of the former is concentrated within 1 eV of the Fermi level, while SMA leads to appreciable density ± 2 eV of the Fermi level (see Figure S1).

These differences can be attributed in part to the unique ways in which each resonant interaction simultaneously modulates the incident optical fields in space and in time. An illustration of spatial confinement associated with each resonance can be seen in the electric field intensity maps at the resonance frequency for the Au LSPR (Figure 1(a)), FP resonance (Figure 1(b)), and WGM resonance (Figure 1(c)); all resonances lead to approximately 1 order of magnitude nearfield enhancement in the vicinity of the Au NC. A progression of resonance lifetimes can be inferred from the extinction spectra of the Au LSPR, the FP resonance, and the WGM resonance, with the Au LSPR having the broadest extinction peak and the shortest lifetime, and the WGM having the most narrow extinction peaks and longest lifetimes. These lifetimes determine the period of time that the metal electrons are being driven by enhanced nearfields associated with the optical resonances, and the long lifetime associated with the WGM means that the nearfield that drives the metal electrons continues to evolve on a relatively long timescale compared to the electronic dynamics. Longevity of the evolution of the electric field resulting from dielectric scattering resonances are consistent with with longer period of population movement from Fermi level and below to higher unoccupied orbitals when compared with surface plasmon resonance of Au.

In contrast to Au, small Pt nanoparticles do not support LSPR at visible wavelengths (see Figure 2 (d)), and consequently, we do not observe any overlap between an absorption resonance of the 2nm Pt NS and the dipole-allowed transitions of our PIW Pt NC model. We also consider the same geometries of the dielectric nanospheres as before ($d = 285\text{nm}$ and

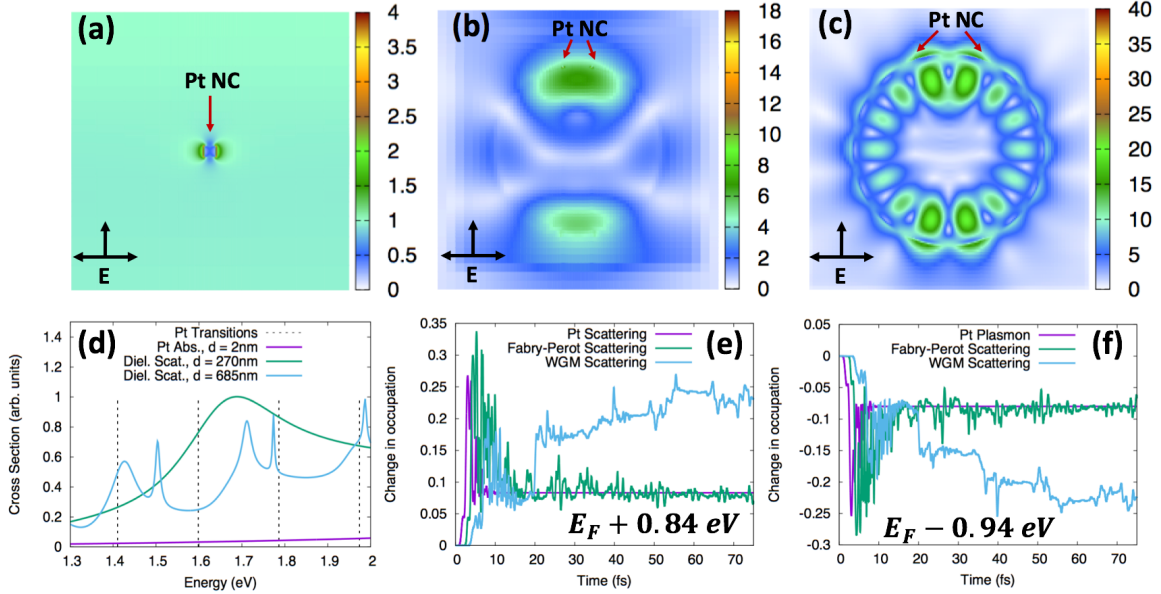


Figure 2: Three regimes for light-matter interactions leading to unique spatial and temporal shaping of the incident field, and the corresponding impact on electronic dynamics in a Pt nanocube. Plots of the near-field enhancements ($|E|/|E_0|$) are shown of the Pt NC's extinction maximum ($\lambda = 200\text{nm}$, **Panel (a)**), a Fabry-Perot resonance of a $d=285\text{nm}$ dielectric nanosphere decorated with Pt NCs ($\lambda = 397\text{nm}$, **Panel (b)**), and a Whispering Gallery Mode resonance of a $d=685\text{ nm}$ dielectric nanosphere decorated with Pt NCs ($\lambda = 493\text{nm}$, **Panel (c)**). The extinction spectra of these three structures are shown overlaid with the dipole-allowed transitions in the PIW model of the Pt NC, showing partial overlap between these transitions and the scattering resonances of the $d=685\text{ nm}$ dielectric nanosphere (**Panel (d)**). The change in orbital populations ($D_p^p(t) - D_p^p(t = 0)$) is computed to measure hot-electron and hot-hole generation. The WGM shows much more efficient generation of hot-electrons (**Panel (e)**) and hot-holes (**Panel (f)**) compared to FP resonance in this case.

$d = 685\text{nm}$); the scattering resonances of the former have partial overlap with transitions in the PIW Pt NC model at 1.6 and 1.8 eV, and the resonances of the latter have partial overlap with transitions at 1.8, 1.8, and 1.95 eV. Again, the dielectric scattering resonances provide approximately an order of magnitude nearfield enhancement in the vicinity of the Pt NC, while the nearfield enhancement provided by the lone Pt NC is much smaller ($|\mathbf{E}|/|\mathbf{E}_0|$ at $\lambda = 200\text{nm}$ corresponding to the extinction maximum, see Figure 2 (a), (b), and (c)). Due to its relatively weak optical interaction, scattering of the Pt NC does not lead to a large density of hot-carriers; small populations of carriers are created near the Fermi energy (see Figure S2). These hot-carriers can be attributed mostly to direct interaction with the incident pulse, which has a peak field strength of $E_0 \approx 614,000,000 \text{ V/m}$, (see Supplemental Information for more details). In this case, SMA on the $d = 285\text{nm}$ nanosphere leads to generation of hot carriers within 1 eV of the Fermi energy with dynamics that persist for moderate (50 fs) timescales. The WGMs supported by the $d = 685$ dielectric NS show much greater efficiency in creating energetic carriers compared to the resonances of the $d = 285\text{nm}$ dielectric NS or the Pt NC. For example, WGMs supported by the $d = 685\text{nm}$ NS are three times more effective at generating holes in the lowest lying orbital ($E_F - 1.6\text{eV}$) and electrons in the highest lying orbital ($E_F + 0.84\text{eV}$) in the PIW Pt NC active space as compared to FP resonance of the $d = 285\text{nm}$ NS (see Figure 2 (e) and (f)). The hot-carriers driven by WGM also show much more persistent dynamics, and continue to evolve beyond 100 fs (see Figure 2 (e) and (f)).

Clear distinction between the three regimes is also observed. The second figure (Figure 4) depicts the scattering spectra of a succession of differently sized dielectric nanospheres and their alignment with the gold dipole-allowed transitions. We observe that the nanosphere with diameter 685nm has the best alignment with the gold transitions, and similarly, the 685nm nanosphere is also most efficient in generating both hot-electrons and hot-holes.

Figure 5 also represents the scattering spectra of a succession of differently sized dielectric nanospheres and their alignment with Pt dipole-allowed transitions. 685nm diameter

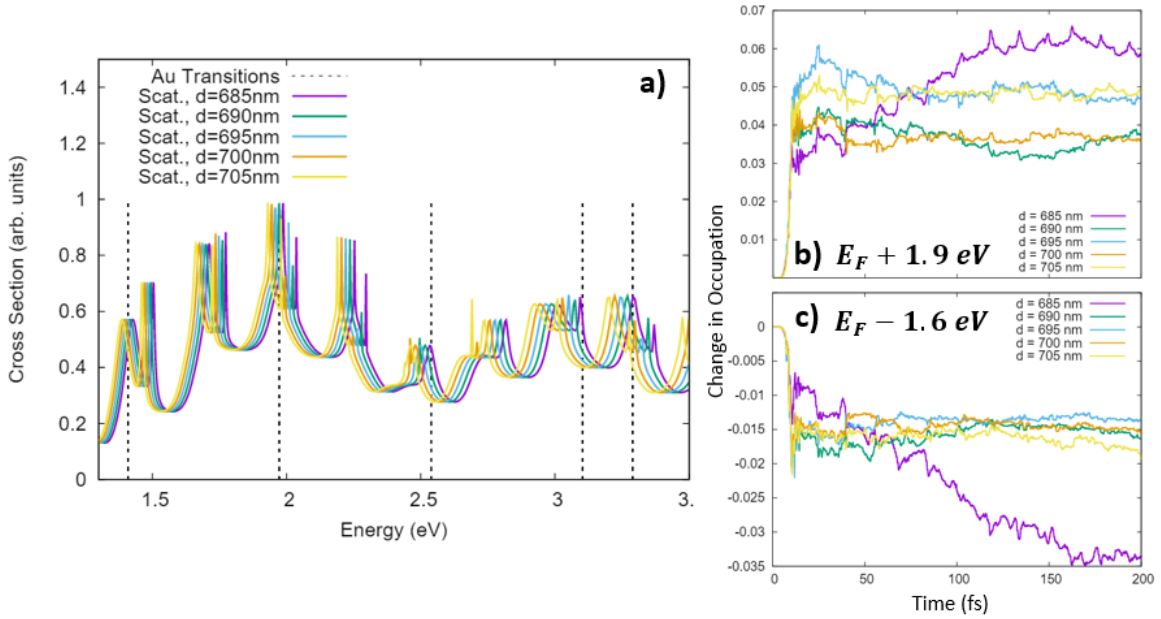


Figure 3: Fine-shaping of the spatial and temporal shaping of the incident field through the geometry of the dielectric nanosphere. Panel (a) shows the scattering spectra of a size progression of dielectric nanospheres that display predominately Whispering Gallery Mode visible resonances. The 685nm nanosphere's scattering spectra has the best overlap with the dipole-allowed transitions in the Au NC model, and this structure shows most efficient generation of hot-electrons in the most energetic orbitals included in our active space (Panel (b)), and more efficiently generation of hot holes in the lowest energy orbitals included in our active space (Panel (c)).

nanospheres display the most accurate alignment with Pt dipole allowed transitions, as was seen in Figure 4 for composite dielectric-Au structures.

The scattering of the dielectric on the spectra compared with the Platinum transitions has a unique significance when compared with the dielectric-Au structure. Although platinum is a non-plasmonic metal in the visible range, it is also capable of generating hot-electrons and hot-holes within the visible light range. This demonstrates this method of hot electron generation is independent of plasmonic activity and potentially can be expanded to various more abundant and cost efficient metals as opposed to Au. The diameter size 685nm is able to excite hot electrons and hot holes on the metal nanocubes on its surface showing its increased efficiency over the rest of the sizes. Extra figures, to be found in the supplemental information accompanying this paper, show the change in occupancy of all the orbitals (with different energies each) in the different structures at various times, for the different metals. (Should we arrange the figures in the supplemental information in groups based upon structure, metal for this paragraph this is how I will arrange them or time step??) We are able to observe in the figures for both metals, that the nanocube cube structures cease to change their orbital occupancy after the 20th timestep. Similarly we find that the Fabry-Perot structures??

Supplementary Information

Plots of Global Hot-Carrier Distributions

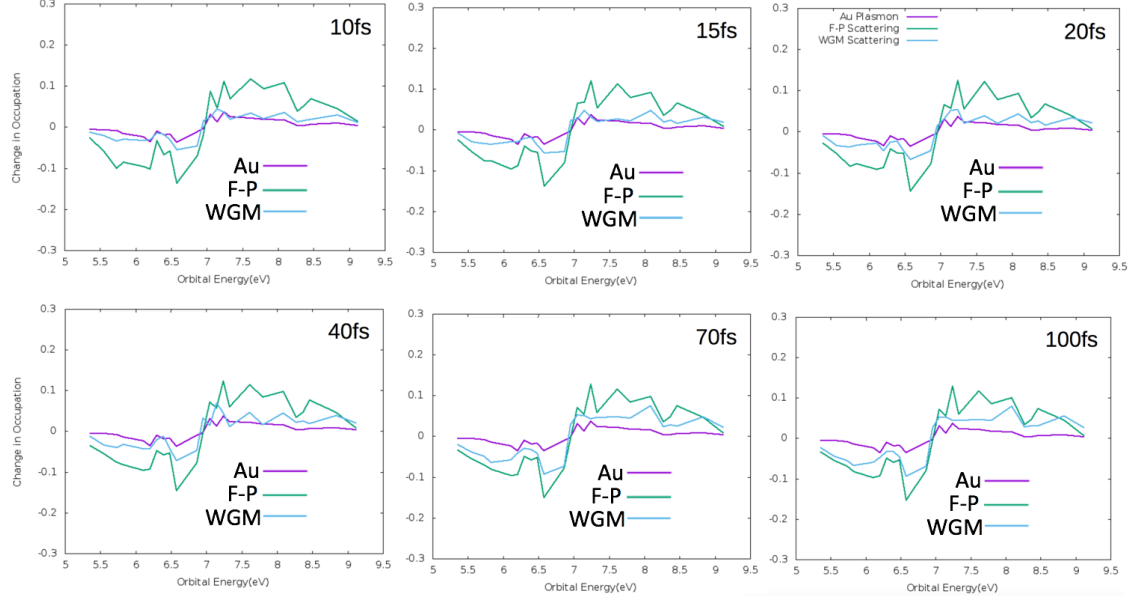


Figure 4: Snapshots of changes in occupation of each orbital in the active space of the PIW Au NC model as a measure of instantaneous hot-carrier distributions. The change in orbital occupation is computed from elements of the time-dependent one-electron reduced density matrix (${}^1\text{RDM}$) relative to their initial value, $D_p^p(t) - D_P^p(t = 0)$ for several timepoints in the simulation.

Electronic structure of metal nanocubes

For cubic metal nanoparticles, we approximate the one-electron orbitals as energy eigenstates of the particle-in-a-cubic-well. For a particle confined by a cubic well with length L , the potential is 0 when $x < L, y < L, z < L$ and infinity otherwise. The energy eigenstates have the form

$$\psi_{nx,ny,nz} = \left(\frac{2}{L}\right)^{3/2} \sin\left(\frac{n_x \pi x}{L}\right) \sin\left(\frac{n_y \pi y}{L}\right) \sin\left(\frac{n_z \pi z}{L}\right). \quad (6)$$

The energy eigenvalues have the form

$$\epsilon_{nx,ny,nz} = \frac{\hbar^2 \pi^2}{2 m L^2} (n_x^2 + n_y^2 + n_z^2). \quad (7)$$

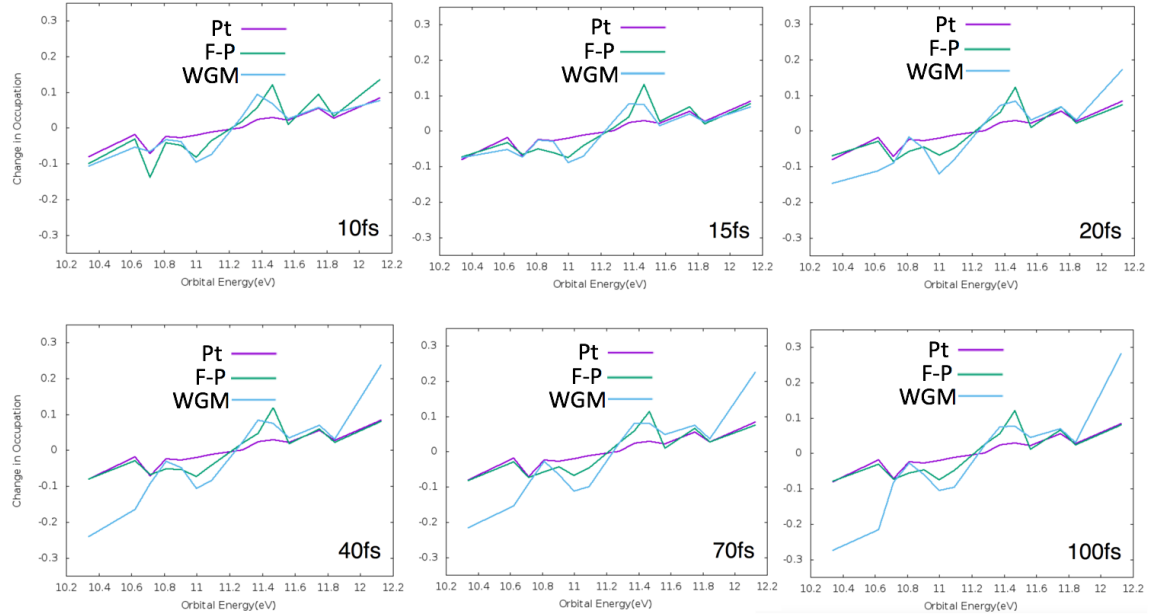


Figure 5: Snapshots of changes in occupation of each orbital in the active space of the PIW Pt NC model as a measure of instantaneous hot-carrier distributions. The change in orbital occupation is computed from elements of the time-dependent one-electron reduced density matrix (^1RDM) relative to their initial value, $D_p^p(t) - D_P^p(t = 0)$ for several timepoints in the simulation.

The transition dipole integrals can be evaluated analytically,

$$\begin{aligned} \langle \psi_{nx,ny,nz} | \hat{\mu}_x | \psi_{nx',ny',nz'} \rangle &= e \delta_{ny,ny'} \delta_{nz,nz'} \frac{L(\pi(n_x - n'_x) \sin(\pi(n_x - n'_x)) + \cos(\pi(n_x - n'_x)) - 1)}{\pi^2(n_x - n'_x)^2} \\ &\quad - e \delta_{ny,ny'} \delta_{nz,nz'} \frac{L(\pi(n_x + n'_x) \sin(\pi(n_x + n'_x)) + \cos(\pi(n_x + n'_x)) - 1)}{\pi^2(n_x + n'_x)^2}, \end{aligned}$$

where $\hat{\mu}_x = -ex$. Analogous expressions can be obtained for expectation values of $\hat{\mu}_y$ and $\hat{\mu}_z$.

We order the orbitals by a single index p such that $\epsilon_{p+1} \geq \epsilon_p$; that is, each $\psi_{nx,ny,nz}$ can be uniquely labeled ψ_q . Using the above expressions and this unique labeling, the diagonal matrix elements can be evaluated as

$$\langle \Phi_0 | \hat{H}(t) | \Phi_0 \rangle = \sum_{p=1}^{nocc} \epsilon_p \quad (8)$$

$$\langle \Phi_i^a | \hat{H}(t) | \Phi_i^a \rangle = \sum_{p=1}^{nocc} \epsilon_p - \epsilon_i + \epsilon_a \quad (9)$$

and the off-diagonal matrix elements can be evaluated as

$$\langle \Phi_0 | \hat{H}(t) | \Phi_i^a \rangle = \langle \psi_i | \mathbf{E}(t) \cdot \hat{\mu} | \psi_a \rangle \quad (10)$$

$$\langle \Phi_i^a | \hat{H}(t) | \Phi_j^b \rangle = \delta_{ij} \psi_a | \mathbf{E}(t) \cdot \hat{\mu} | \psi_b \rangle - \delta_{ab} \psi_i | \mathbf{E}(t) \cdot \hat{\mu} | \psi_j \rangle. \quad (11)$$

Finite-difference time-domain calculations

A commercial simulator based on the finite-difference time-domain method²⁸ was used to compute the electric field, $E(t)$ 1 Å away from the nanoparticle surface in each of the scenarios considered. The displacement was taken along the z -axis, corresponding to the polarization direction of incident light since the strongest near-field enhancement is expected along this direction. A grid spacing of 1 Å in x , y , and z was utilized in a cubic region extending 1 nm beyond the metal NP surface, and a non-uniform mesh was utilized otherwise with dx , dy ,

$dz \leq 20\text{nm}$. For each composite structure, a nanoparticle was placed at the surface of the dielectric nanosphere at an angle of 20° with respect to the propagation axis of the incident light. In all simulations, light propagates along the x axis and is polarized along the z axis. The metal nanoparticles are centered at $y = 0$. A total-field scattered-field source was used to illuminate the structures. The FDTD simulations were terminated when the ratio of the total energy in the simulation volume to the total energy injected by the illumination source falls below 10^{-6} . Because the WGMs are higher quality factor resonances, longer time is typically required for these simulations as compared to the plasmonic particles alone.

The resulting time-domain fields were fed into our TDCIS algorithm, allowing us to simulate the electronic dynamics driven by rigorously-computed nearfields from scattering and plasmon resonances, which show strong spatiotemporal modification relative to freely propagating light. The electric field was scaled by a factor $E_0 \approx 614,000,000 \text{ V/m}$ so that the peak power of the illumination source is 10^{15} W/m^2 . The electric field was sampled at intervals of approximately 2.8 attoseconds for all simulations, which leads to a time-step that ensures stability of the wavefunction propagation with the relevant energy scales of our simulations. Our TDCIS scheme requires the evaluation of the electric field at intermediate times between these timesteps, and we use a simple update based on centered-finite differences to approximate the electric fields at these times. As an example, if the electric field is known at times t_1 , $t_2 = t_1 + dt$, and $t_3 = t_1 + 2 \cdot dt$ where $dt = 2.8 \text{ as}$, and knowledge of the field is required at some time $t_m = t_2 + m \cdot dt$ where m is non-integer, $E(t_m)$ is estimated as follows:

$$\mathbf{E}(t_m) = \mathbf{E}(t_2) + \frac{\mathbf{E}(t_3) - \mathbf{E}(t_1)}{t_3 - t_1} \cdot m \cdot dt. \quad (12)$$

The optical response of Au and Pt in the FDTD simulations utilizes permittivity data from the work of Johnson and Christy³¹ and Palik,³² respectively. We assume a static dielectric constant of 2.6 for the dielectric nanospheres in this work, which is comparable to the visible dielectric constant of titanium dioxide.

Acknowledgment

This work was performed, in part, utilizing resources at the Center for Nanoscale Materials, a US Department of Energy, Office of Science, Office of Basic Energy Sciences User Facility (contract no. DE-AC02-06CH11357). JJF Acknowledges the College of Science and Health for startup support. J.C. and N.E. acknowledge the NSF-GS-LSAMP for support. K.F. acknowledges the WPU CFR for support. †J.C., N.E., and K.F. contributed equally to this work.

References

- (1) Linic, S.; Christopher, P.; Ingram, D. B. Plasmonic-metal nanostructures for efficient conversion of solar to chemical energy. *Nat. Mater.* **2011**, *10*, 911921.
- (2) Kale, M. J.; Avanesian, T.; Christopher, P. Direct Photocatalysis by Plasmonic Nanostructures. *ACS Catalysis* **2013**, *4*, 116–128.
- (3) Zhou, N.; López-Puente, V.; Wang, Q.; Polavarapu, L.; Pastoriza-Santos, I.; Xu, Q.-H. Plasmon-enhanced light harvesting: applications in enhanced photocatalysis, photodynamic therapy and photovoltaics. *RSC Adv.* **2015**, *5*, 29076.
- (4) Park, J. Y.; Kim, S. M.; Lee, H.; Nedrygailov, I. I. Hot-electron-mediated surface chemistry: toward electronic control of catalytic activity. *Acc. Chem. Res.* **2015**, *48*, 2475.
- (5) Atwater, H. A.; Polman, A. Plasmonics for improved photovoltaic devices. *Nature Mater.* **2010**, *9*, 205–213.
- (6) Sun, Y.; Xia, Y. Shape-controlled synthesis of gold and silver nanoparticles. *Science* **2002**, *298*, 21762179.

- (7) Burda, C.; Chen, X.; Narayanan, R.; El-Sayed, M. A. Chemistry and properties of nanocrystals of different shapes. *Chem. Rev.* **2005**, *105*, 10251102.
- (8) Gramotnev, D. K.; Bozhevolnyi, S. I. Plasmonics beyond the diffraction limit. *Nature Photon.* **2010**, *4*, 8391.
- (9) Christopher, P.; Xin, H.; Linic, S. Visible-light-enhanced catalytic oxidation reactions on plasmonic silver nanostructures. *Nature Chem.* **2011**, *3*, 467472.
- (10) Marimuthu, A.; Zhang, J.; Linic, S. Tuning selectivity in propylene epoxidation by plasmon mediated photo-switching of Cu oxidation state. *Science* **2013**, *339*, 1590–1593.
- (11) Mukherjee, S.; Libisch, F.; Large, N.; Neumann, O.; Brown, L. V.; Cheng, J.; Lasiter, J. B.; Carter, E. A.; Nordlander, P.; Halas, N. J. Hot Electrons Do the Impossible: Plasmon-Induced Dissociation of H₂ on Au. *Nano Letters* **2013**, *13*, 240–247.
- (12) Li, Z.; Foley IV, J. J.; Peng, S.; Sun, C.-J.; Ren, Y.; Wiederrecht, G. P.; Gray, S. K.; Sun, Y. Reversible Modulation of Surface Plasmons in Gold Nanoparticles Enabled by Surface Redox Chemistry. *Angew. Chem.* **2015**, *127*, 9076–9079.
- (13) Zhang, N.; Han, C.; Xu, Y.-J.; Foley IV, J. J.; Zhang, D.; Codrington, J.; Gray, S. K.; Sun, Y. Near-field dielectric scattering promotes optical absorption by platinum nanoparticles. *Nat. Photon.* **2016**, *10*, 473–482.
- (14) Zhang, J.; Jin, X.; Morales-Guzman, P. I.; Yu, X.; Liu, H.; Zhang, H.; Razzari, L.; Claverie, J. P. Engineering the Absorption and Field Enhancement Properties of Au-TiO₂ Nanohybrids via Whispering Gallery Mode Resonances for Photocatalytic Water Splitting. *ACS Nano* **2016**, *10*, 4496–4503.
- (15) Swearer, D. F.; Zhao, H.; Zhou, L.; Zhang, C.; Robatjazi, H.; Martirez, J. M. P.; Krauter, C. M.; Yazdi, S.; McClain, M. J.; Ringe, E. et al. Heterometallic antennare-

actor complexes for photocatalysis. *Proceedings of the National Academy of Sciences* **2016**, *113*, 8916–8920.

- (16) Sousa-Castillo, A.; Comesaa-Hermo, M.; Rodrguez-Gonzlez, B.; Prez-Lorenzo, M.; Wang, Z.; Kong, X.-T.; Govorov, A. O.; Correa-Duarte, M. A. Boosting Hot Electron-Driven Photocatalysis through Anisotropic Plasmonic Nanoparticles with Hot Spots in AuTiO₂ Nanoarchitectures. *The Journal of Physical Chemistry C* **2016**, *120*, 11690–11699.
- (17) Govorov, A. O.; Zhang, J.; Gun'ko, Y. K. Theory of photoinjection of Hot Plasmonic Carriers from Metal Nanostructures into Semiconductors and Surface Molecules. *J. Phys. Chem. C* **2013**, *117*, 16616–16631.
- (18) Sundararaman, R.; Narang, P.; Jermyn, A. S.; Goddar III, W. A.; Atwater, H. A. Theoretical predictions for hot-carrier generation from surface plasmon decay. *Nat. Commun.* **2014**, *5*, 5788.
- (19) Wu, K.; Chen, J.; McBride, J. R.; Lian, T. Efficient hot-electron transfer by a plasmon-induced interfacial charge-transfer transition. *Science* **2015**, *349*, 632.
- (20) Ma, J.; Wang, Z.; Wang, L.-W. Interplay between plasmon and single-particle excitations in a metal nanocluster. *Nat. Commun.* **2015**, *6*, 10107.
- (21) Brown, A. M.; Sundararaman, R.; Narang, P.; Goddard III, W. A.; Atwater, H. A. Nonradiative Plasmon Decay and Hot Carrier Dynamics: Effects of Phonons, Surfaces, and Geometry. *ACS Nano* **2016**, *10*, 957–966.
- (22) Kraus, W. A.; Schatz, G. C. Plasmon resonance broadening in small metal particles. *J. Chem. Phys.* **1983**, *79*, 61306139.
- (23) Zhang, H.; Govorov, A. O. Optical Generation of Hot Plasmonic Carriers in Metal

Nanocrystals: The Effects of SHape and Field Enhancement. *J. Phys. Chem. C* **2014**, *118*, 7606–7614.

- (24) Manjavacs, A.; Liu, J. G.; Kulkarni, V.; Nordlander, P. Plasmon-Induced Hot Carriers in Metallic Nanoparticles. *ACS Nano* **2014**, *8*, 7630–7638.
- (25) Kumarasinghe, C. S.; Premaratne, M.; Bao, Q.; Agrawal, G. P. Theoretical analysis of hot electron dynamics in nanorods. *Sci. Rep.* **2015**, *5*, 12140.
- (26) Saavedra, J. R. M.; Asenjo-Garcia, A.; García de Abajo, F. J. Hot-Electron Dynamics and Thermalization in Small Metallic Nanoparticles. *ACS Photonics* **2016**, *0*, null.
- (27) Bernardi, M.; Mustafa, J.; Neaton, J. B.; Louie, S. G. Theory and computation of hot carriers generated by surface plasmon polaritons in noble metals. *Nat. Commun.* **2015**, *6*, 7044.
- (28) Lumerical Solutions, Inc., <http://www.lumerical.com/tcad-products/mode/>.
- (29) Sanz-Serna, J. M.; Portillo, A. Classical numerical integrators for wave-packet dynamics. *J. Chem. Phys.* **1996**, *104*, 2349–2355.
- (30) Bohren, C. F.; Huffman, D. R. *Absorption and Scattering of Light by Small Particles*; John Wiley and Sons, 1998.
- (31) Johnson, P. B.; Christy, R. W. Optical constants of noble metals. *Phys. Rev. B* **1972**, *6*, 4370.
- (32) Palik, E. D. *Handbook of optical constants of solids*; Academic Press, 1998.